Supporting Information

# Origin of Unexpected Products from $CO_2$ Electroreduction on Silver: The Role of ppb-level Copper Impurity in the Electrolyte

Chaoqun Ma[1,2], Flora Haun[1,2], Federico Dattila[3], Wankai Tang[1,2], Gumaa A. El-Nagar[1], Ajin Anilkumar[1,2], Simelys Hernández[3], Matthew T. Mayer[1,2*]

1 Electrochemical Conversion, Helmholtz-Zentrum Berlin für Materialien und Energie GmbH, Hahn-Meitner Platz 1, 14109 Berlin, Germany

2 Institute für Chemie und Biochemie, Freie Universität Berlin, 14195 Berlin, Germany

3 CREST Group, Department of Applied Science and Technology (DISAT), Politecnico di Torino, Corso Duca degli Abruzzi 24, 10129, Turin, Italy

***Corresponding Author**

E-mail: m.mayer@helmholtz-berlin.de

# Table of Contents

**Supplementary Note 1**

In these experiments, constant potentials (vs Ag/AgCl reference electrode) were applied without *iR* correction, leading to the possibility that the actual electrode potential varied between measurements in different electrolyte concentrations. Indeed, as shown in Table S1 the uncompensated solution resistance ($R_U$) varied inversely with ionic strength. However, the resulting currents ($i$) varied directly with the concentration, and therefore post-correcting the applied potential by Ohm's law ($E = iR_U$) revealed that variation of the corrected potential ($E_{cor}$) from 0.3 M to 1 M $KHCO_3$ was rather minor. We observed that under 0.1 M $KHCO_3$ the *iR* drop is largely different from others. In order to compare the selectivity at same unpurified 0.1 M electrolyte condition with and without *iR* correction, we did one control experiment with 85% *iR* correction (Figure 1f). It shows a detectable $CH_4$ signal starting from 1 h, then slowly becomes more pronounced. Nevertheless, the selectivity is not as high as from 0.5 M condition, even though the Cu contamination level is comparable around 2 μg/L, and CO also mainly dominant overall. This observation suggests that the higher selectivity at 0.1 M $KHCO_3$ with 85% *iR* correction could be resulted from a more negative overpotential and higher current density which promotes the $CH_4$ generation. We advise on the use of *iR* correction to avoid these discrepancies, even though there is lack of standardize protocols, and the opportunity for misuse, regarding such corrections.[1-3]

Table S1. Summary of electrochemical parameters corresponding to the experiments of Figure 1. $CO_2R$ conducted at -2.1 V vs. Ag/AgCl (uncorrected) in $CO_2$-saturated electrolyte of varied $KHCO_3$ concentrations (unpurified), with $R_u$ determined by potentiostatic EIS, the initial measured current density $i$, the resulting *iR* drop, the corresponding post-corrected potentials vs. Ag/AgCl, the measured pH, and corresponding post-corrected potentials on the RHE scale.

| $C(KHCO_3)$ [M] | $R_u$ [Ω] | $i_{initial}$ [mA] | *iR* [mV] | $E_{Ag/AgCl}$-*iR* [V] | pH | $E_{RHE}$-*iR* [V] |
|---|---|---|---|---|---|---|
| 0.1 M | 66.12 | -7.21 | -476.7 | -1.62 | 6.75 | -1.02 |
| 0.3 M | 26.48 | -13.40 | -354.8 | -1.75 | 7.16 | -1.13 |
| 0.5 M | 18.28 | -18.01 | -329.2 | -1.77 | 7.37 | -1.14 |
| 0.7 M | 11.79 | -22.92 | -270.2 | -1.83 | 7.54 | -1.19 |
| 1.0 M | 5.85 | -30.14 | -176.3 | -1.92 | 7.72 | -1.27 |

## Additional experimental data

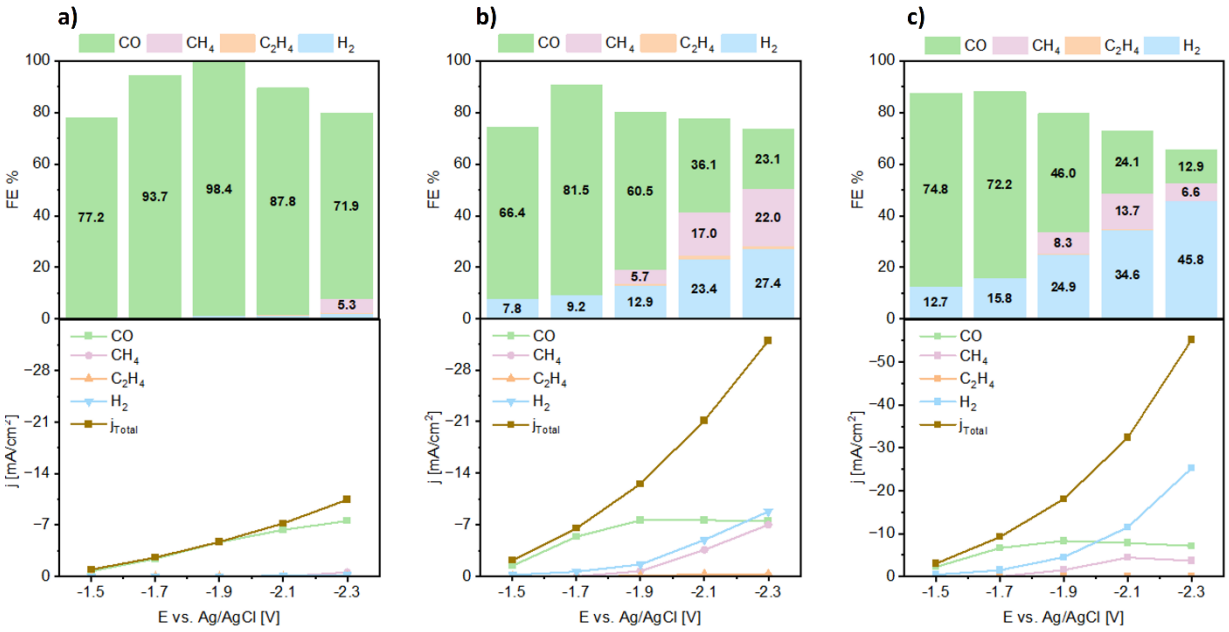


Figure S1**.** The faradaic efficiency (top) and partial current density (bottom) of CO, $CH_4$, $C_2H_4$ and $H_2$ under potentiostatic operation on polished Ag foil with 1 $cm^2$ geometric surface area, stepped periodically to increasingly large overpotentials, with repeated GC injections at each condition. Electrolyte concentrations (unpurified) were **a)** 0.1 M, **b)** 0.5 M, and **c)** 1 M $KHCO_3$, tested under continuous $CO_2$ bubbling. (Liquid products omitted, but shown in Figure 1g in the maintext).

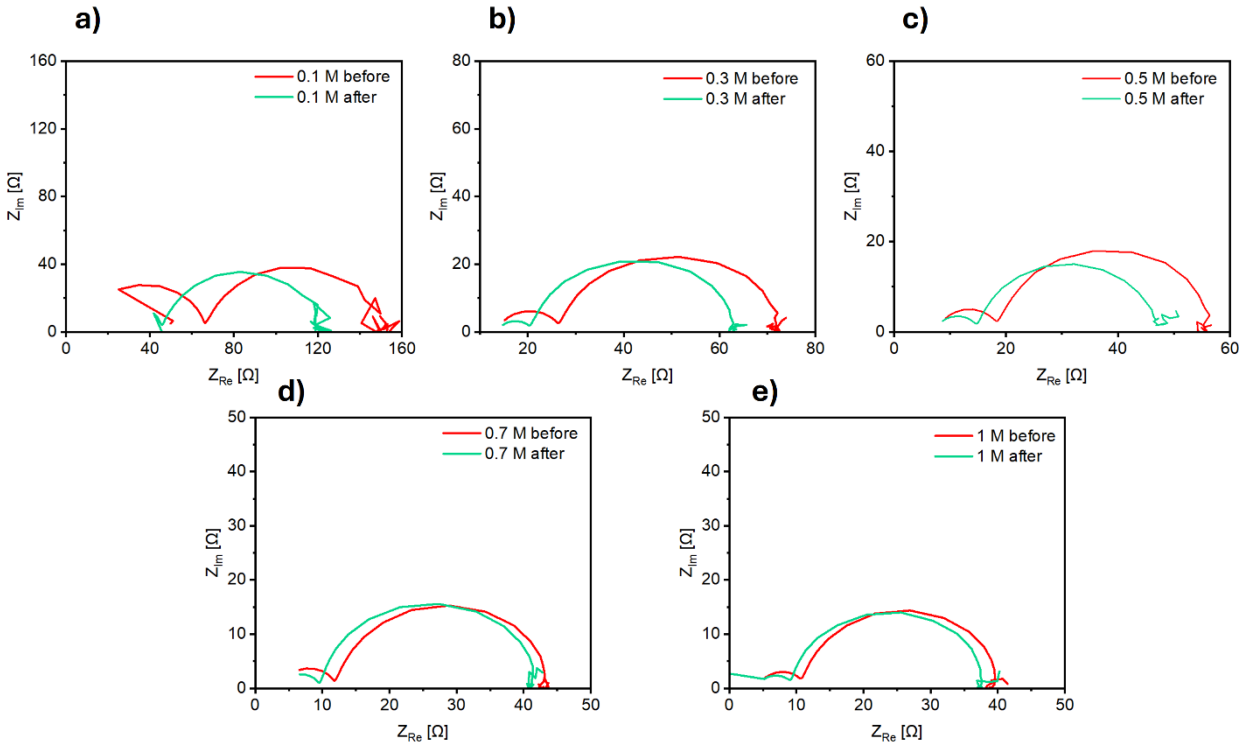


Figure S2. Nyquist plots from potentiostatic EIS measurements from the experiments of Figure 2 at electrolyte concentration of **a)** 0.1 M, **b)** 0.3 M, **c)** 0.5 M, **d)** 0.7 M, and **e)** 1 M. The PEIS were conducted at -1.51 V vs. Ag/AgCl (chosen to be near the current onset potential) with a frequency range 200 kHz to 100 mHz, both before and after each 3 h $CO_2R$ experiment. A clear shift towards lower uncompensated resistance was observed in all cases, suggesting an increased conductivity in the electrolyte.

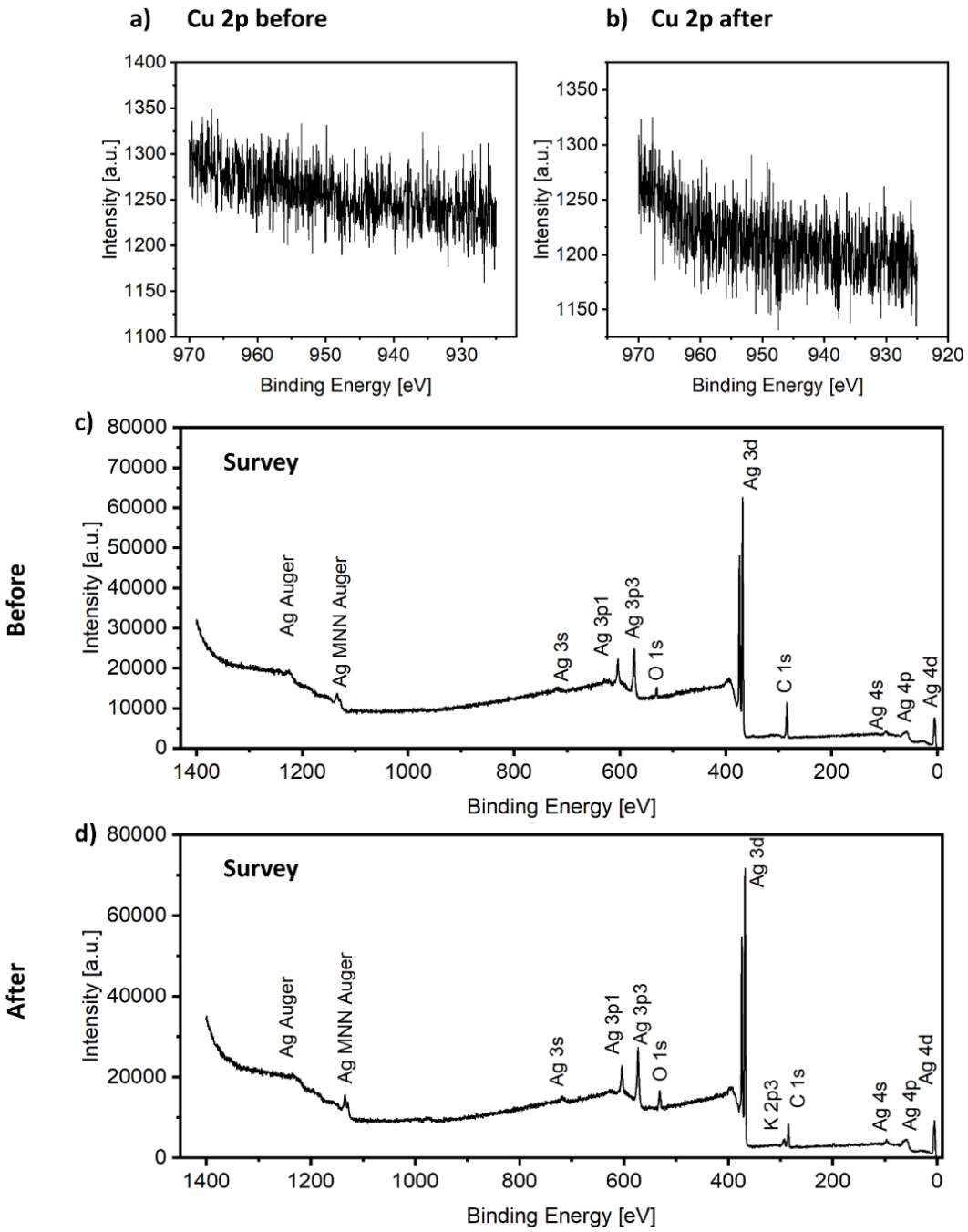


Figure S3. XPS spectra of Ag foil electrodes before and after $CO_2R$ experiments conducted in unpurified 0.5 M $KHCO_3$ at $E_{Ag/AgCl}$ = -2.1 V for 3 h. The electrode was taken out from the electrolyte after the full electrochemical sequence, rinsed by ultra-pure water, dried and transferred to the XPS analysis chamber. **a, b)** Cu 2p core-level scans showed no detectable Cu signals. **c, d)** Survey scans of the Ag foil before and after full sequence of electrochemical test.

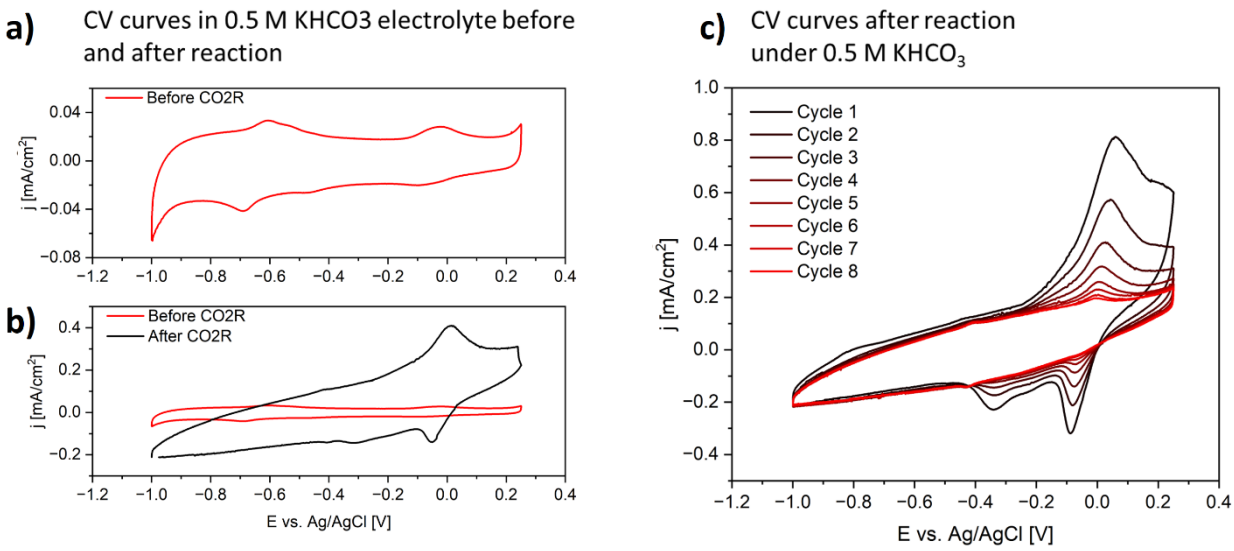


Figure S4. **a)** Cyclic voltammetry of Ag in $CO_2$ bubbled unpurified 0.5 M $KHCO_3$ before the chronoamperometry experiment (the data was taken from the 10$^{th}$ cycle following repeated cycling). **b)** Comparison of cyclic voltammetry of Ag in 0.5 M $KHCO_3$ before and after the chronoamperometry experiment. The CV curve was taken from the 4$^{th}$ cycle, and the shape of the CV change is shown in **c)**. The CVs are from the data set from the experiment of Figure 1, 0.5 M case. All CVs were recorded at potential sweep rate of 200 mV/s.

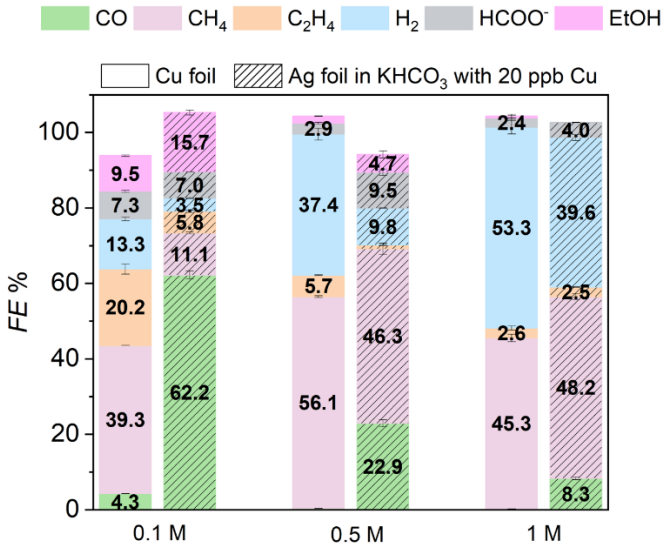


Figure S5. Faradaic efficiency distribution of $CO_2$ reduction products on Cu foil electrodes in purified $KHCO_3$ electrolytes (0.1, 0.5, and 1 M), compared with Ag foil electrodes under identical concentration electrolyte conditions with 20 ppb Cu added.

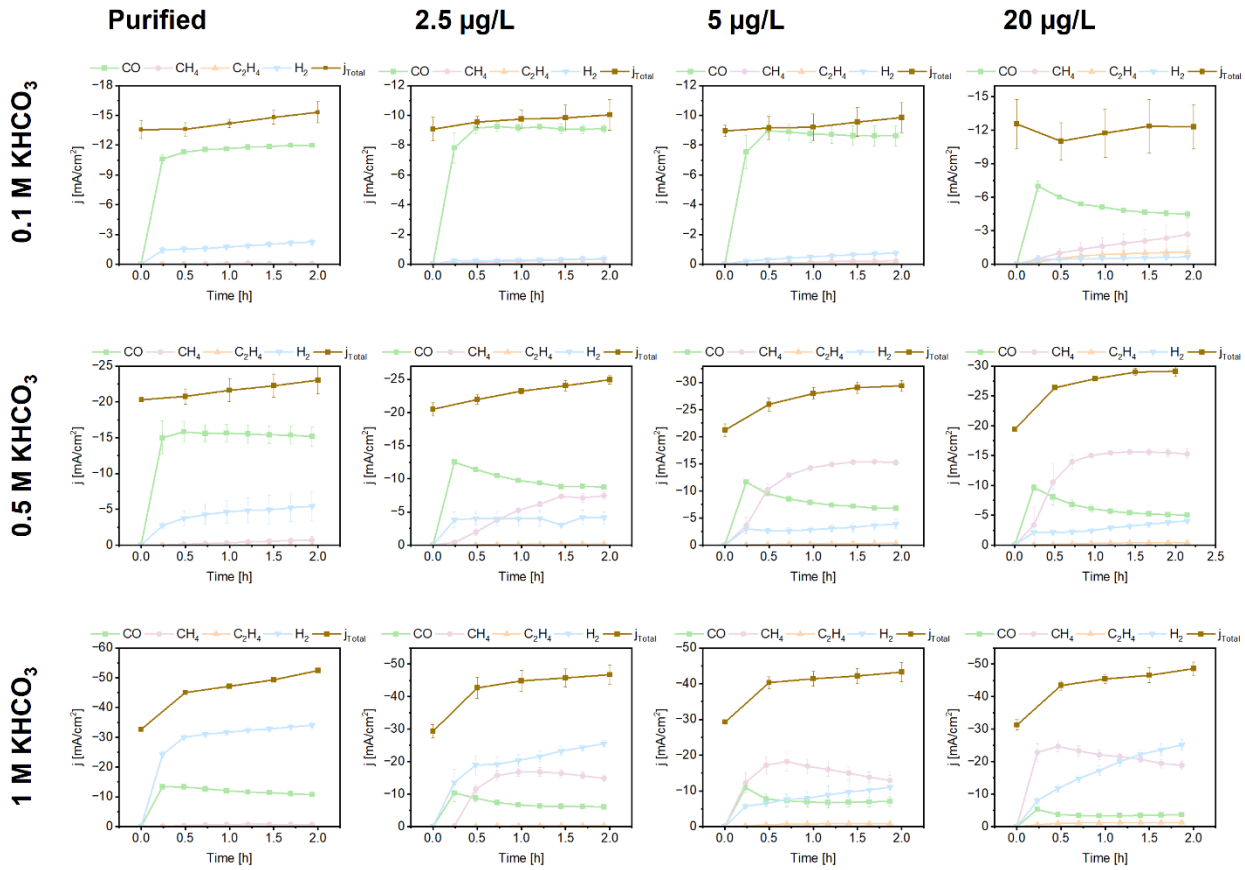


Figure S6. Averaged measured current densities ($j_{total}$) and partial current densities of gaseous products from $CO_2R$ on Ag under different electrolyte conditions. All experiments were performed at $E_{Ag/AgCl} = -2.1$ V without *iR* correction. For partial current density, each data point corresponds to one GC injection, and the partial current densities were calculated from the concentration of the respective gaseous products. Representative total current densities were obtained from the EC data at 0, 0.5, 1, 1.5, and 2 h, and subsequently averaged. Error bars represent the standard deviation from duplicate experiments using freshly $CO_2$ purged electrolytes and freshly polished Ag foil electrodes. These data were used to calculate the Faradaic efficiencies shown in Figure 2.

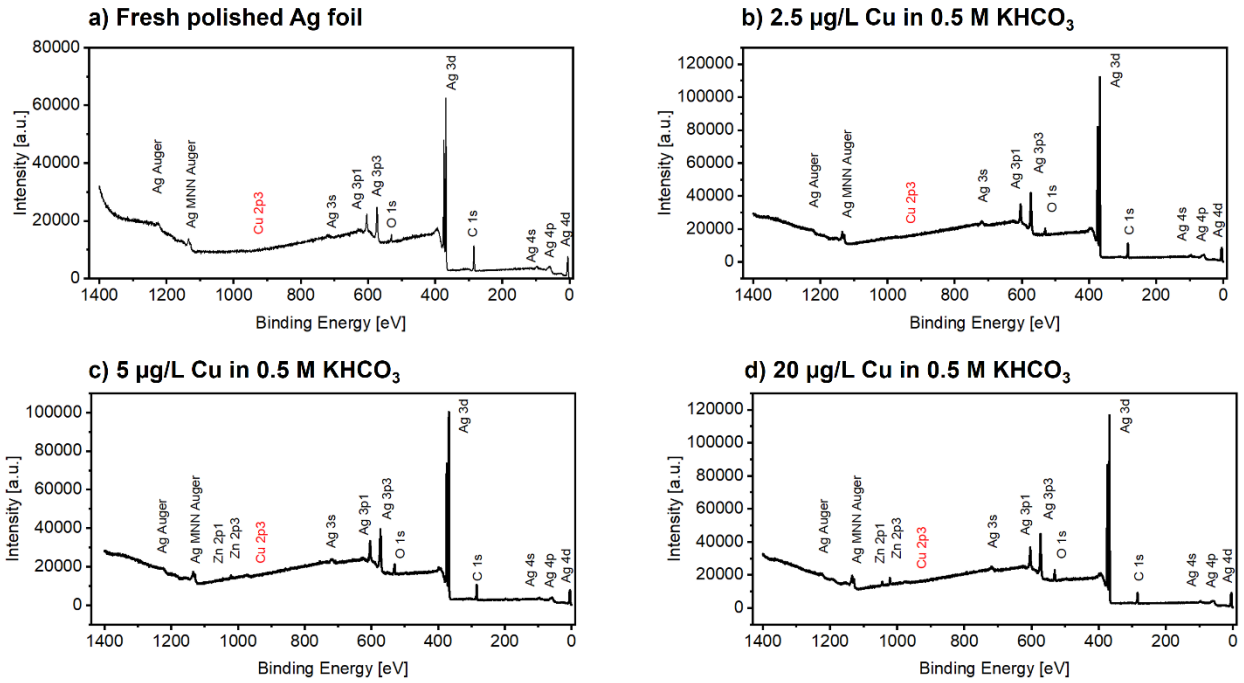


Figure S7. Complementary survey XPS spectra on Ag foil before and after experiment conducted at 0.5 M $KHCO_3$ with different Cu content at $E_{Ag/AgCl}$ = -2.1 V for 2 hours. The electrode was withdrawn from the electrolyte under applied potential. The surface was rinsed with several droplets of ultra-pure water before measuring XPS. **a-d)** show no detectable Cu signals either before or after the experiment, indicating that the polished Ag foil surface was free of contamination. Moreover, it suggests that XPS is insufficient to confirm the existence of ppb-level Cu impurity unless a better-defined method, e.g., ambient pressure XPS can be employed. We observed signals contributed by Zn impurities, which are aligned with our observation from the Zn stripping feature on the CVs.

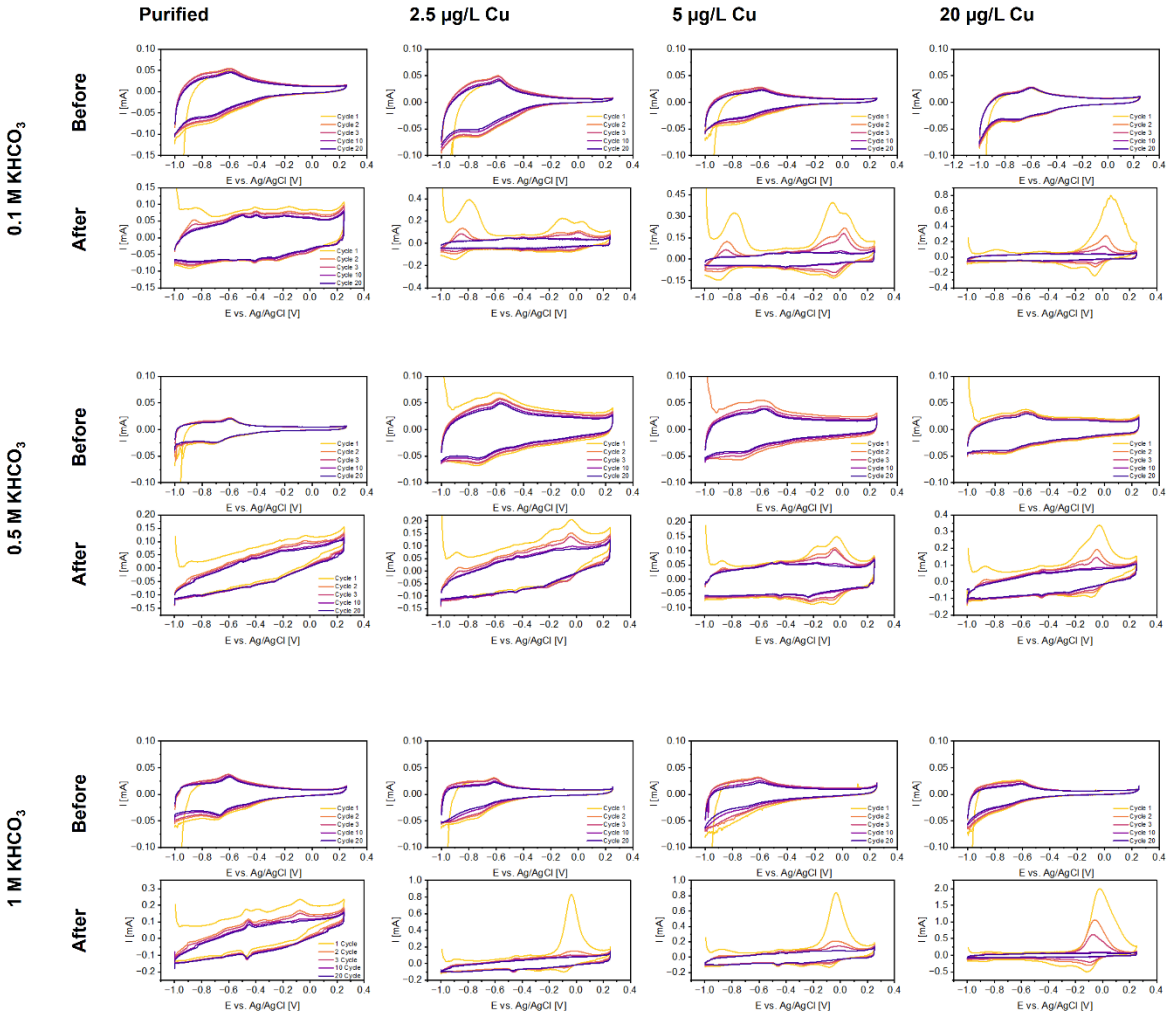


Figure S8. Cyclic voltammetry on Ag foil before and after $CO_2R$ experiments in different electrolyte concentrations (left labels) with different Cu impurity levels (top labels). Scan rate: 200 mV/s. In each case 20 CV cycles were performed, and here for clarity we only show cycles 1-3, 10, and 20.

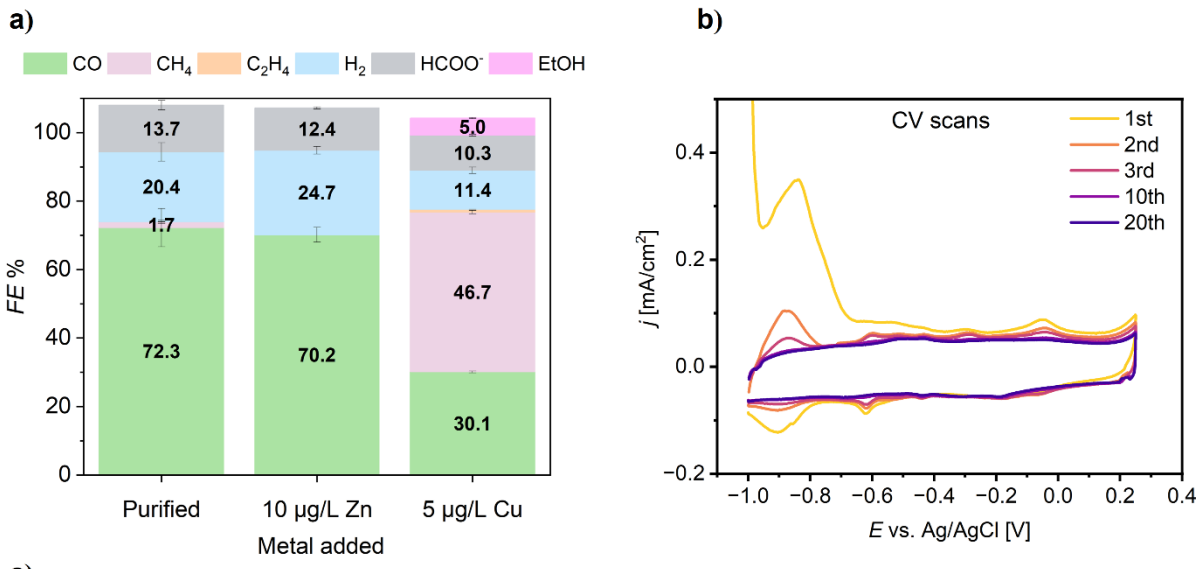


c)

| *Experiment* | *C(Zn) from ICP-OES at 213.856 nm* |
|---|---|
| 10 µg/L Zn in 0.5 M $KHCO_3$ | 10.904 µg/L |

Figure S9**.** Influence of Zn impurities on $CO_2R$. **a)** Product distribution over three experimental conditions: Chelex purified 0.5 M $KHCO_3$, 10 µg/L Zn ($ZnCl_2$) doped in purified 0.5 M $KHCO_3$, and 5 µg/L Cu doped in purified 0.5 M $KHCO_3$. **b)** CV scans of an Ag foil electrode after a 2 h electrolysis in 0.5 M $KHCO_3$ containing 10 µg/L Zn. **c)** Zn ion concentration in the 10 µg/L doped electrolyte before electrolysis, determined by ICP-OES.

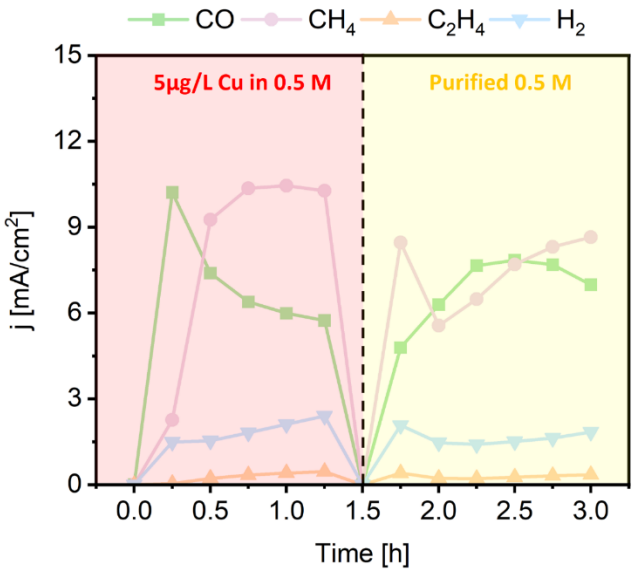


Figure S10**.** Control experiment showing a polished Ag foil first operated in 0.5 M $KHCO_3$ with 5 µg/L Cu contamination for ~1.5 h, followed by electrolyte replacement with fresh purified electrolyte solution while maintaining the applied potential. Partial recovery of $CH_4$ activity suggests that residual Cu remained on the Ag surface during the electrolyte swap.

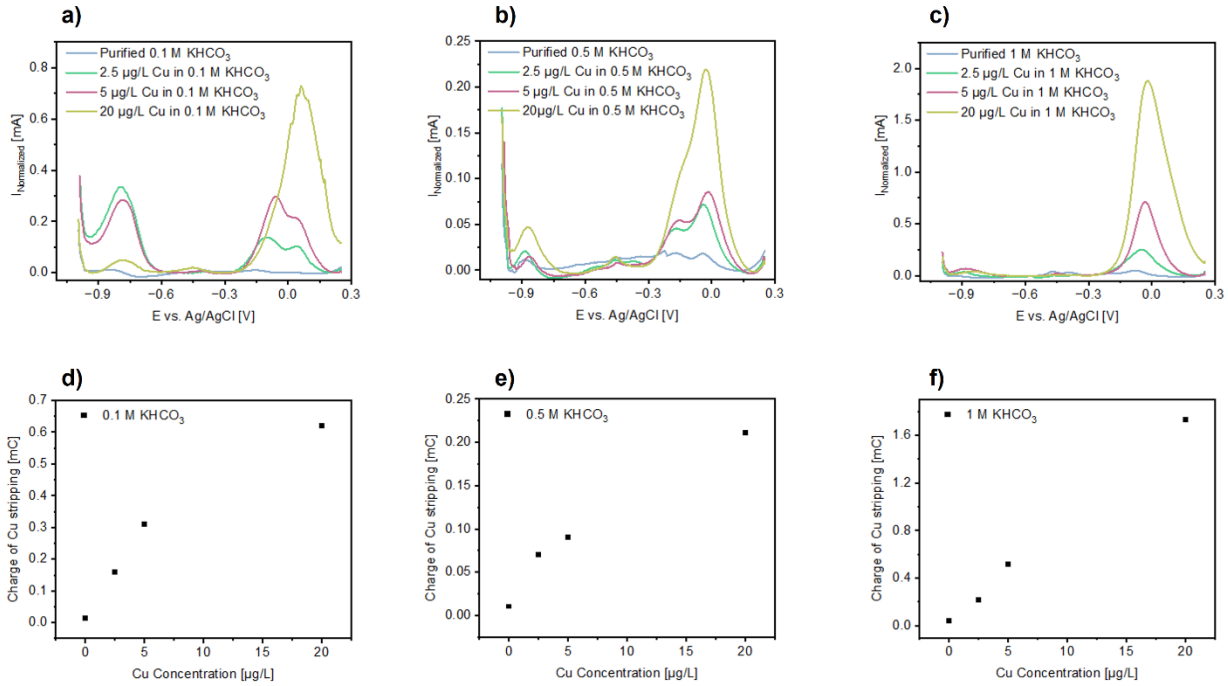


**Figure S11.** Cyclic voltammetry characterization of Ag foil electrodes after $CO_2R$ testing. **(a-c)** Baseline-normalized cyclic voltammograms (first scan) recorded in 0.1 M, 0.5 M, and 1 M $KHCO_3$ with different Cu contents. **(d–f)** Scatter plots of added Cu concentration in the electrolyte and the integrated charge of the stripping peak between -0.3 to 0.3 V vs. Ag/AgCl from **(a-c)** (respectively), showing clear correlation. All CVs acquired from the experiment sets from Figure 2.

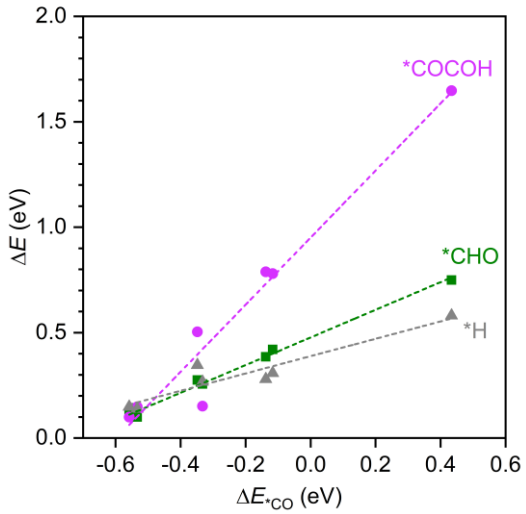


**Figure S12.** Linear scaling relationships between *H (gray), *CHO (green), *COCOH (purple) formation energies vs CO formation energy on Ag(111) p(3×3), Cu(111) p(3×3), $Cu_{ML}Ag(111)$ p(3×3), $Cu_{ML}Ni(111)$ p(3×3), $Cu_{ML}Pd(111)$ p(3×3), $Cu_{ML}Pt(111)$ p(3×3), $Cu_{ML}Au(111)$ p(3×3). Fitting parameters reported in Table S7.

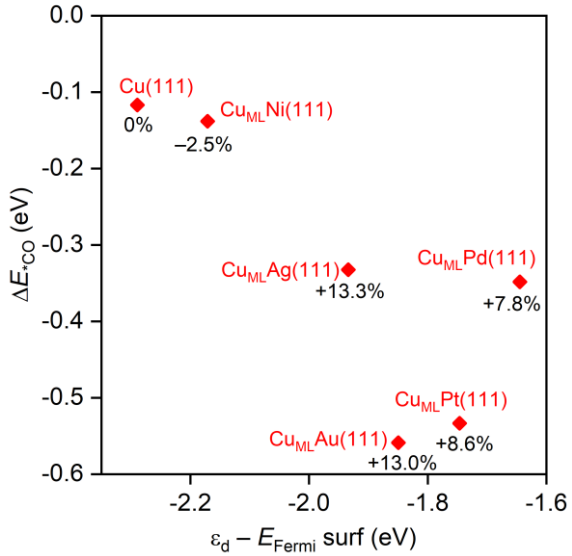


**Figure S13.** Dependence of CO formation energy on *d*-band center of surface Cu atoms for different $Cu_{ML}M(111)$ systems (labelled in red). Black labels indicate substrate-induced strain on Cu surface atoms, described by the lattice mismatch between Cu monolayer and substrates.

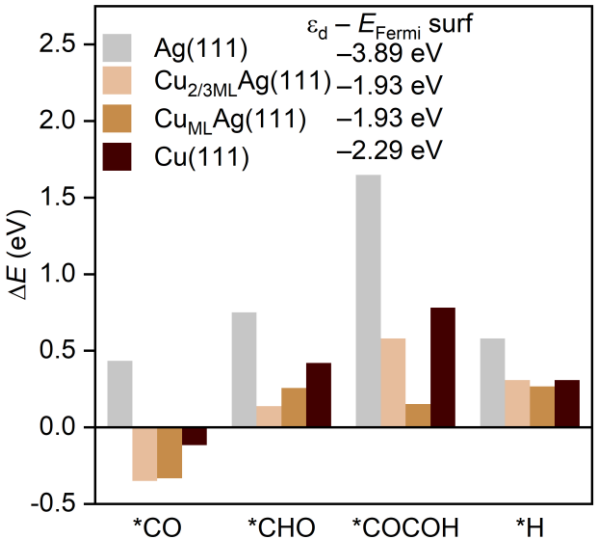


**Figure S14.** Comparison of *CO, *CHO, *COCOH, and *H formation energies on Ag(111) p(3×3), $Cu_{2/3ML}Ag(111)$ p(3×3), $Cu_{ML}Ag(111)$ p(3×3), Cu(111) p(3×3).

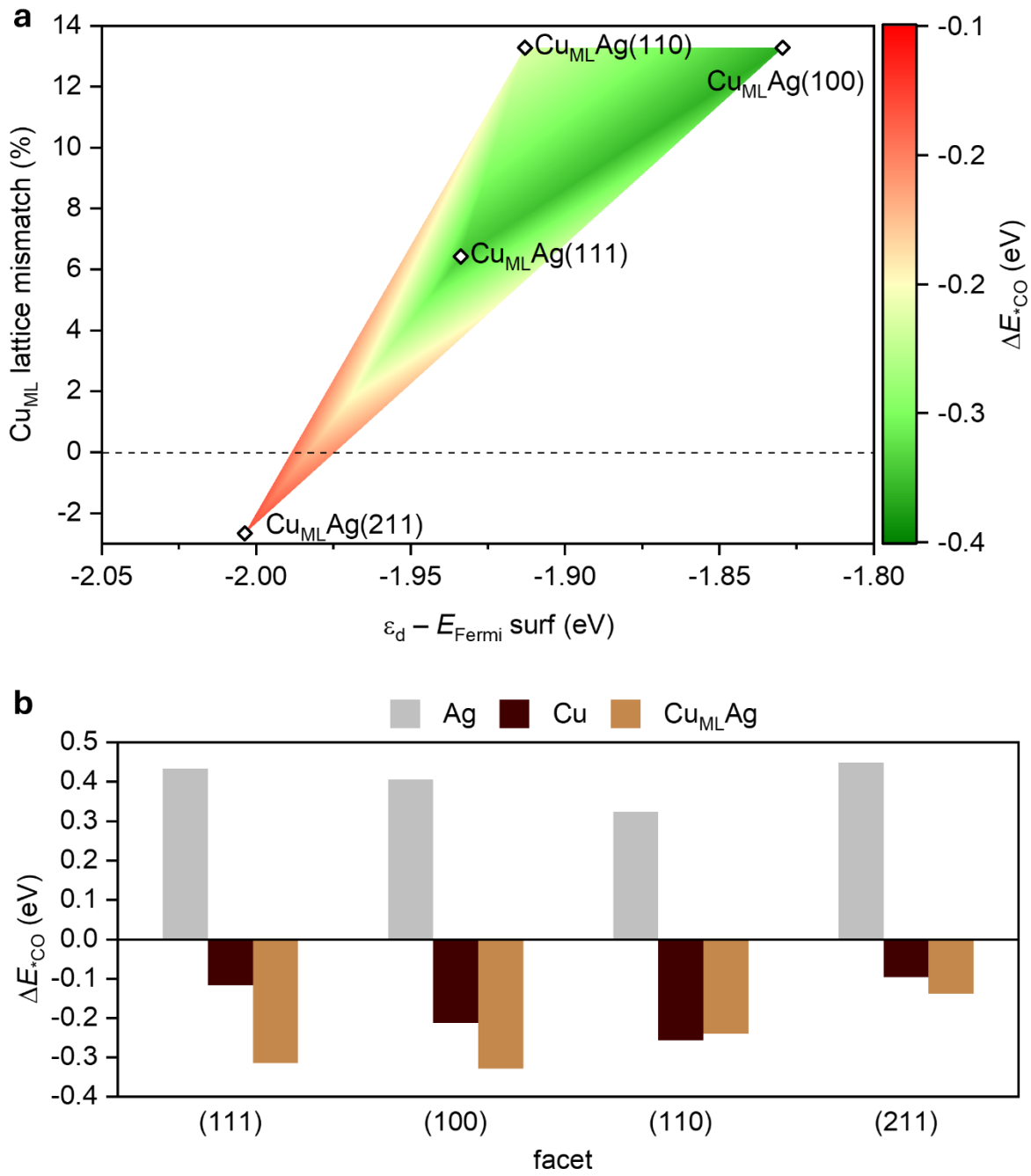


**Figure S15: a)**, CO formation energy (color scale) vs d-band center of the surface layer (x-axis) and lattice mismatch (y-axis) on different $Cu_{ML}Ag$ facets. **b)** Comparison of *CO formation energies on different Ag, Cu, $Cu_{ML}Ag$ facets.

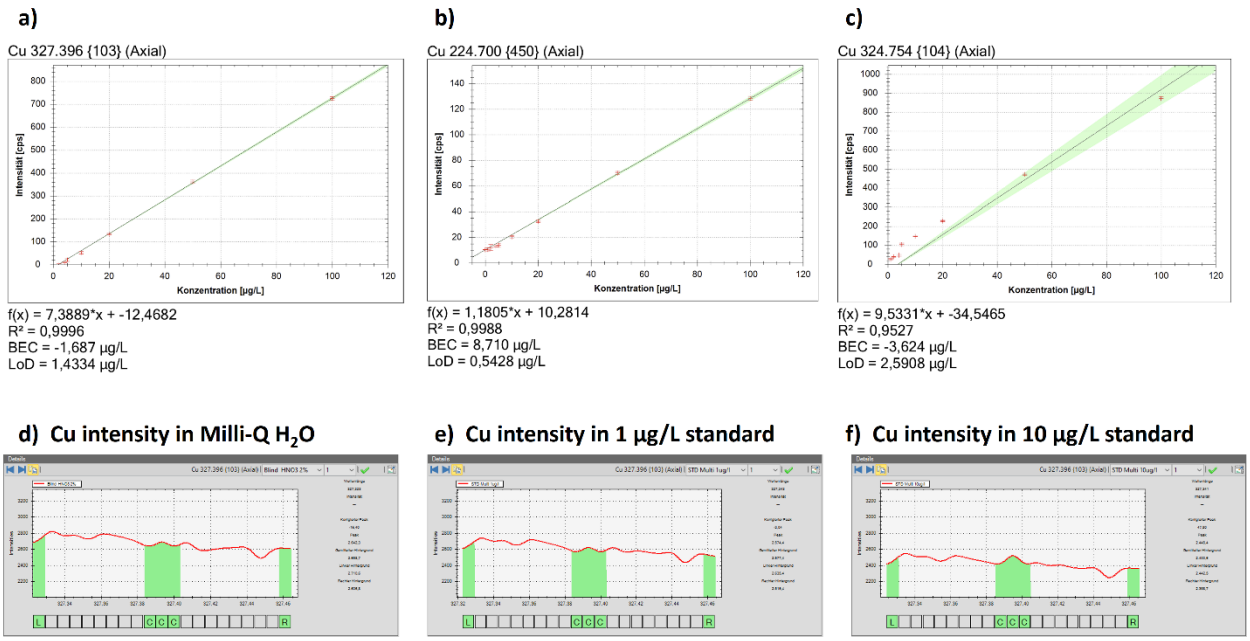


**Figure S16** ICP-OES calibration curves of Cu obtained at three wavelengths: **a)** 327.396 nm, **b)** 224.700 nm, and **c)** 324.754 nm. Among them, the 327.396 nm calibration curve exhibited the best linear fit with the lowest error. Therefore, Cu contamination levels were determined using this wavelength. **d)**, **e)**, and **f)** show the spectra recorded for Milli-Q water, the ICP standard at 1 µg/L, and the ICP standard at 10 µg/L, respectively. A background peak is clearly visible in the Milli-Q water at 327.396 nm, which leads to reduced accuracy for measurements below 10 µg/L.

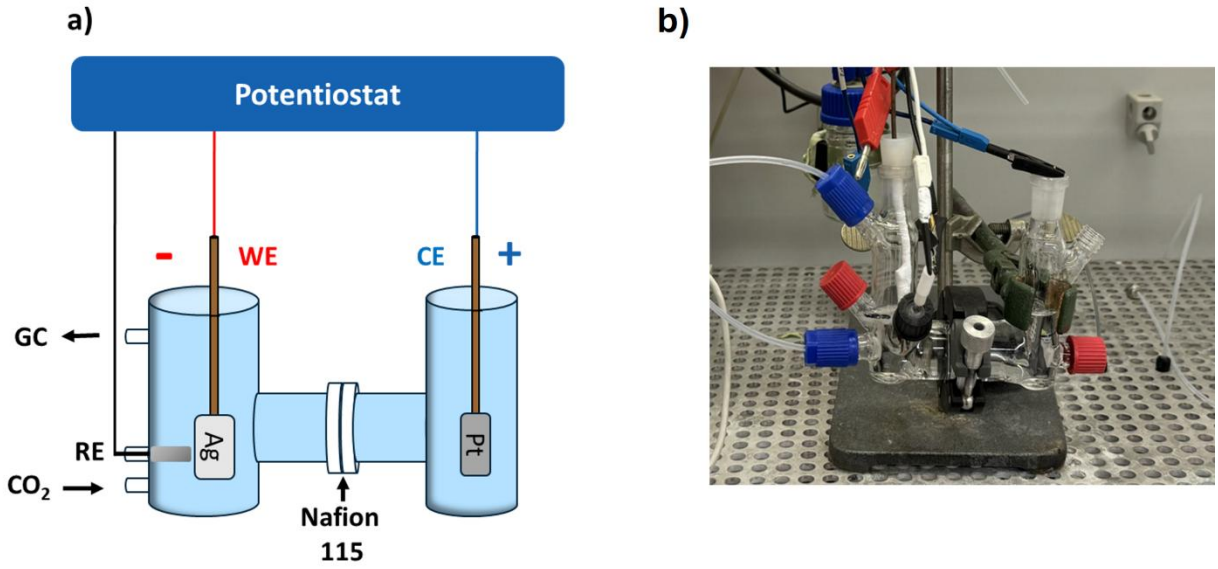


**Figure S17.** **a)** Graphic and **b)** photo of the electrochemical cell used.

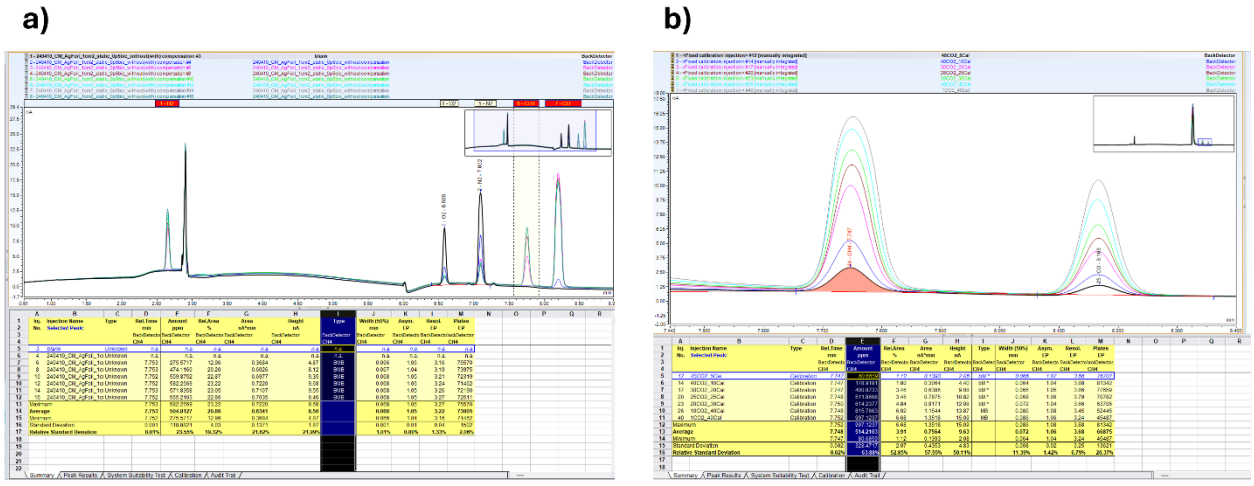


**Figure S18. a)** GC chromatogram of the experiment conducted at $CO_2$ bubbled unpurified 0.5 M $KHCO_3$ at -2.1 V constant potential for 3 h. The chromatogram shows no $H_2$/$CH_4$/CO impurities from $CO_2$ gas stream or anywhere besides $CO_2R$ reaction. **b)** GC calibration chromatograms within the range of 100 ppm to 1000 ppm.

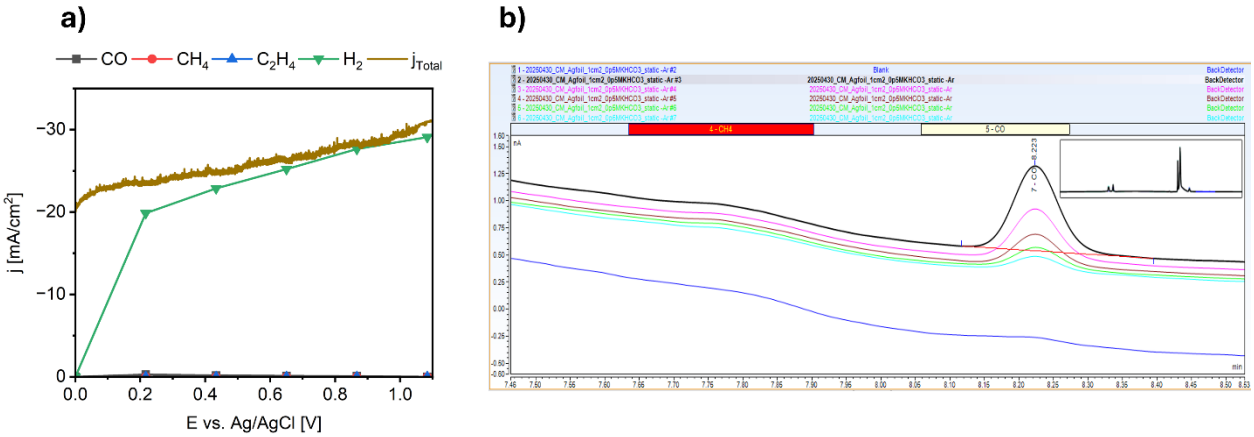


**Figure S19.** The control experiment was conducted using Ag foil in unpurified 0.5 M $KHCO_3$ under Ar bubbling conditions. **a)** shows only $H_2$ was detected as the predominant product. **b)** confirms that no $CH_4$ signal was observed on the GC, demonstrating that $CH_4$ detected under $CO_2$ bubbling conditions is not contributed from system impurities. Chromatograms demonstrated with different colors from black to light blue represent the sequence of measurements.

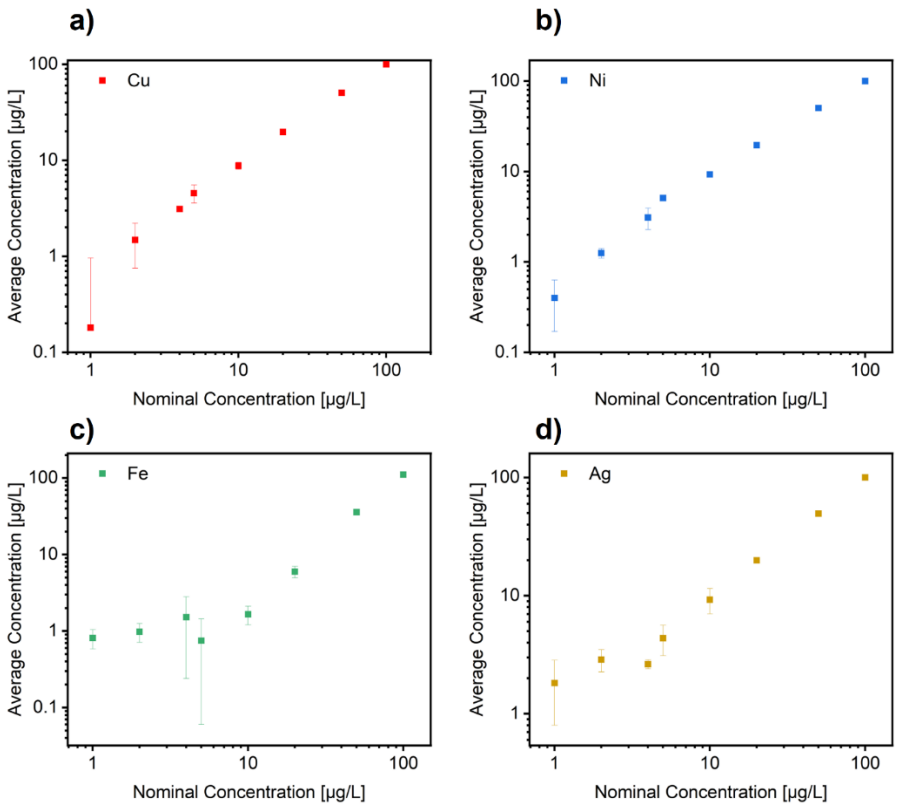


**Figure S20.** ICP-OES measurements of **a)** Cu, **b)** Ni, **c)** Fe, and **d)** Ag calibration standards (measured at wavelengths 324.754, 231.604, 259.940, and 338.289 nm, respectively). For each concentration, three replicate measurements were performed, and the standard deviation was derived from these replicates. For measurements of Cu at levels at or below 2 µg/L the standard deviation is relatively large (≥50%) due to the influence of the background spectrum (see Figure S21).

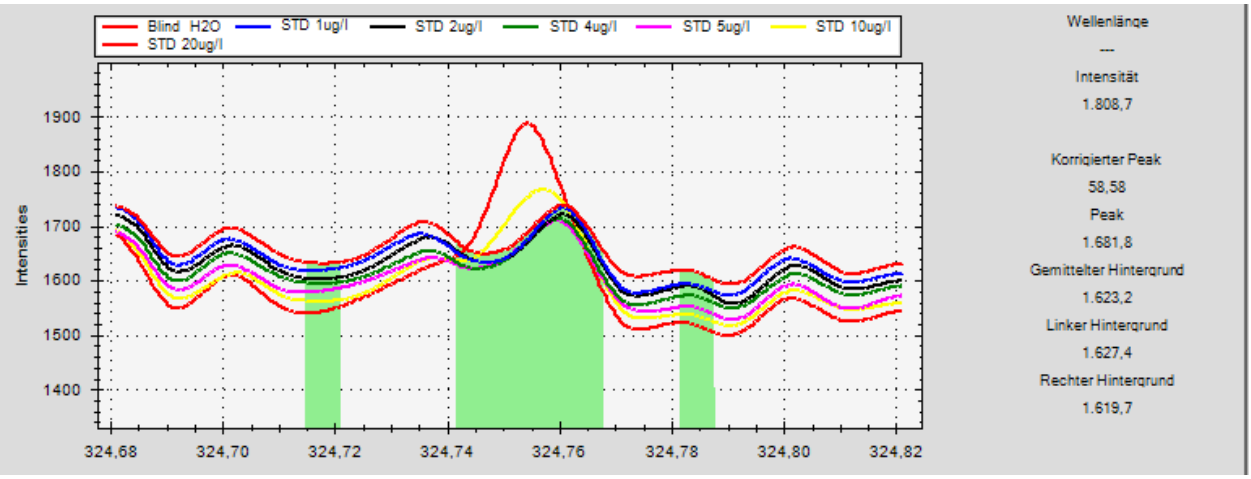


**Figure S21.** ICP-OES spectrum around 324.75 nm obtained using Cu standards ranging from 1 to 20 µg/L.

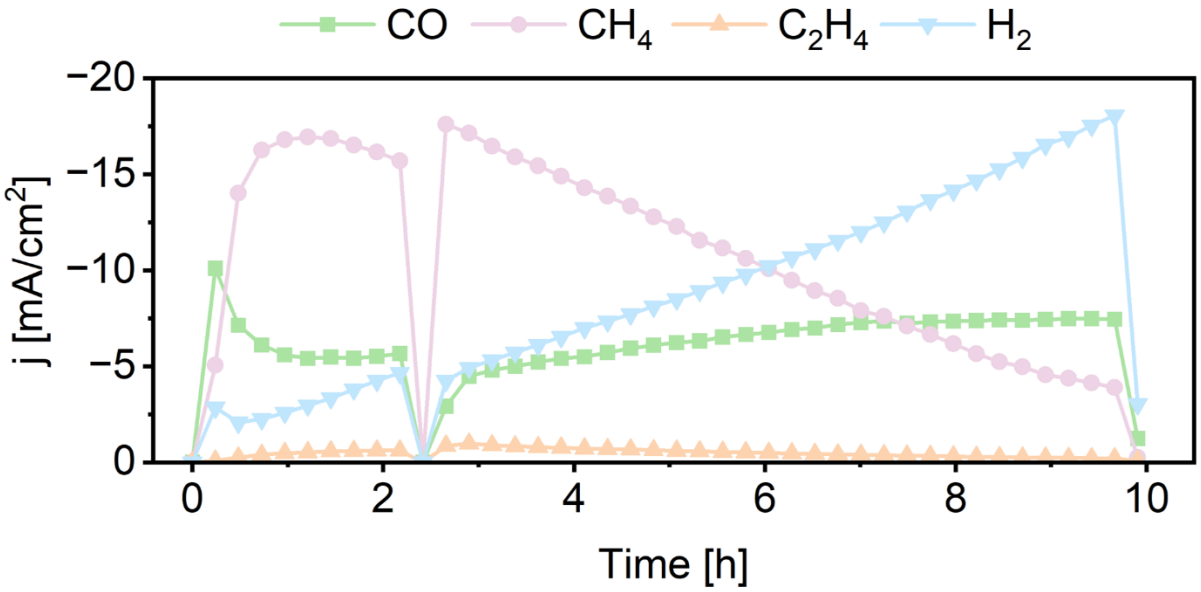


**Figure S22.** 10 h $CO_2R$ experiment on Ag in 0.5 M $KHCO_3$ containing 5 ppb Cu impurity. The electrolysis was paused at ~2 h, with the cell held at OCP for 2 min. The experiment was terminated after 10 h because continuous $K^+$ crossover diluted the anolyte, increased the anolyte resistance, and eventually led to unstable cell operation.

**Supplementary Note 2**

The time-resolved $CO_2R$ data reveal how activity and selectivity vary over time during the experiments, for tests conducted in both unpurified (Figure 1) and purified (Cu-free, Figure S6) electrolytes. In each case, both the measured current density and $j(H_2)$ increase monotonically with time, while the $j$(CO), by contrast, gradually decreases. These dynamic behaviors underscore the importance of conducting experiments over extended durations, and raise questions about the origin of these phenomena.

From electrochemical impedance spectroscopy (EIS) measurements before and after each chronoamperometry experiment, we observed a clear decrease in the uncompensated series resistance ($R_U$, Figure S2), suggesting an increase in electrolyte conductivity over time. Suspecting this may signal changes to the electrolyte composition, we assessed the dissolved $K^+$ content in the cathode chamber (catholyte) before and after 2 h $CO_2R$ at varying $KHCO_3$ concentrations, using ICP-OES. Table S2 presents, for a set of $CO_2R$ experiments conducted in 3 different starting $KHCO_3$ concentrations, the electrolyte $C(K^+)$ measured by ICP-OES before ($C_K^{init}$) and after ($C_K^{final}$) electrochemical testing, the volume of catholyte before starting the experiment ($V_{cat}^{init}$) and the volume change due to $H_2O$ transport ($\Delta V_{cat}$), the measured electrical charge passed in each experiment ($Q_e$), and the resulting calculated transference number for the $K^+$ ion ($t_K$) based on the ratio of moles of $K^+$ and $e$ passed during the experiment. The $K^+$ ions are thus major charge-carrying ions in this system, accounting for ca. 62% of the charge in each experiment. Therefore, to relate our $CO_2R$ results to the actual concentration over time, we used the following relation to determine the actual concentration $C(K)$ per the following equation:

$$C(K) = C_K^{init} + \frac{\Delta n_K}{V} = C_K^{init} + \frac{Q \cdot t_K}{V \cdot F}$$

This calculation was applied to convert $Q$ to $C$(K) for the experiments shown in Figure 5b.

**Table S2.** Measured catholyte concentrations before and after experiments, catholyte volume changes due to $H_2O$ movement, charge passed, and calculated transference number for $K^+$ ion transport during three experiments using different starting $KHCO_3$ electrolyte concentrations.

| $V_{cat}^{init}$ [L] | $C_K^{init}$ [mol/L] | $\Delta V_{cat}$ [L] | $C_K^{final}$ [mol/L] | $\Delta n_K$ [mol] | $Q_e$ [C] | $\Delta n_e$ [mol] | $t_K = \frac{\Delta n_K}{\Delta n_e}$ | $pH_{before}$ | $pH_{after}$ |
|---|---|---|---|---|---|---|---|---|---|
| 0.025 | 0.087 | -0.074e-3 | 0.108 | 5.17e-4 | 80.25 | 8.32e-4 | 0.621 | 6.75 | 6.93 |
| 0.025 | 0.473 | +0.189e-3 | 0.516 | 1.17e-3 | 167.39 | 1.74e-3 | 0.674 | 7.37 | 7.47 |
| 0.025 | 0.991 | +0.406e-3 | 1.079 | 2.64e-3 | 337.72 | 3.50e-3 | 0.754 | 7.72 | 7.80 |

$$\Delta n_K = C_K^{final} \cdot (V_{cat.}^{init} + \Delta V_{cat.}) - C_K^{init} \cdot V_{cat.}^{init}$$

$$\Delta n_e = Q_e / F \quad (F = 96485 \text{ C/mol})$$

As shown in Table S2, in each case, there was a noticeable increase in $K^+$ concentration $C(K^+)$ after the experiment, likely due to transport from anode to cathode compartment. By relating

the $K^+$ molar increase to the total electrical charge passed , we determined transference number values for $K^+$ ($t_K$) as charge carrier from anolyte to catholyte, finding values in between 0.62~0.75. This indicates that $K^+$ (and not only $H^+$) is a major charge-carrying ion in this system, leading to significant changes in electrolyte ion distribution over time. This phenomenon is enabled when using a cation exchange membrane and a near-neutral solution in which the alkali cation concentration is far higher than that of free $H^+$, resulting in facile $K^+$ transport through the membrane. While the inert $K^+$ moves from anolyte to catholyte, the charge balance is maintained by the conversion of $HCO_3^-$ to $CO_2$ in the acidic environment near the anode, and by generation of $HCO_3^-$ from reaction of $CO_2$ in the alkaline environment near the cathode.

The schematic Figure S21a summarizes the processes occurring in the cell. Considering those factors, it is, in retrospect, not surprising to observe this phenomenon (which was also recently reported by Zheng et al[4]), but we feel this behavior has often been overlooked in literature on $CO_2R$ employing cation exchange membranes, possibly inadvertently contributing to selectivity changes during extended experiments.

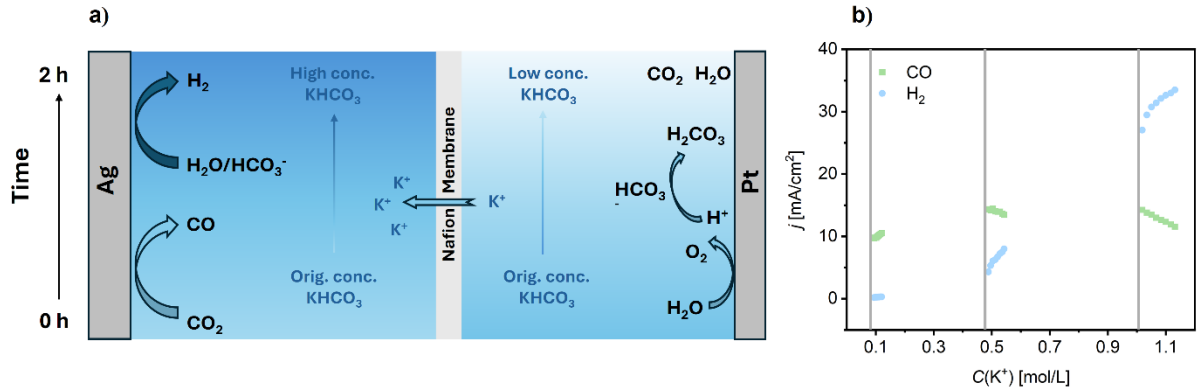


**Figure S23.** a) Schematic illustration of electrode processes, cation migration, and its influence on $CO_2R$ selectivity over time in $CO_2$-purged purified $KHCO_3$ electrolytes. b) Production rates of CO and $H_2$ from on-line gas analysis, as a function of real-time $C(K^+)$ during $CO_2R$ at -2.1 V, using three different initial electrolyte concentrations. Vertical lines indicate the starting conditions, and subsequent gas sample analyses over time progress to the right due to continuous enrichment of $K^+$ in the catholyte . The data were obtained from new, independent experiments distinct from previous results. Only the time-resolved products (gases) are depicted, in order to relate them to the continuous electrolyte changes. Liquid products cannot be assessed with this time resolution in these experiments due to the detection limits of the HPLC.

Since the $C(K^+)$ is dynamic over the course of an experiment, we further refined our analysis of purified electrolyte experiments by calculating the real-time concentration of catholyte $C(K^+)$ as described in and re-plotted the partial current densities of major gaseous products against $C(K^+)$ (Figure S21b). This analysis provides additional detail on the electrolyte dependence of selectivity toward different products. Namely, $j(H_2)$ shows a striking direct correlation across the concentration range. In contrast, $j$(CO) was rather invariant across a wide range of $C(K^+)$, with values ranging from 10-14 mA/cm². In the 0.5 M and 1 M experiments, $j$(CO) increased rapidly to a maximum and then gradually decreased over time (similar to both Figure 1 and Figure S6). This suggests that in the initial minutes of testing, regardless of the original electrolyte concentration, Ag always exhibits high activity for CO production.

However, in contrast to $H_2$, which increases with $C(K^+)$, the CO selectivity dropped over time during each measurement.

As discussed earlier, the mechanistic origins of electrolyte-dependent $CO_2R$ selectivity have been the subject of numerous studies which show that a broad range of phenomena are influenced by the type and concentration of electrolyte ions. Here, our results uniquely reveal possible concentration effects that dynamically affect the relative selectivity between CO and $H_2$. While we do not endeavor here to present a detailed mechanistic understanding of these results, we note that the recent multiscale modelling study of Lorenzutti, et al.[5] provides a strong basis for interpreting our observed dependence of selectivity on electrolyte concentration. Their model predicted a strong direct correlation between $j(H_2)$ and $C(K^+)$, as observed across our experiments. Regarding $j$(CO), the situation is more complex due to competing phenomena. For instance, while a higher concentration of $K^+$ can facilitate the formation of more $CO_2R$ active sites (microenvironments) on the Ag surface, cation accumulation can eventually limit $CO_2$ transport due to steric effects. Dynamic variations in local pH may also play a partial role in the selectivity evolution. However, in similar $KHCO_3$-based cell configurations the catholyte pH has been reported to remain relatively stable since the $KHCO_3$ electrolyte provides buffering capacity. The difference of pH values from our experiments measured before and after experiments showed increases of 0.1~0.2 pH units (See Table S2), which is expected due to increased electrolyte concentration, suggesting that both ionic strength and pH changes may together influence the selectivity changes. Furthermore, $CO_2$ transport is also negatively influenced by its decreased solubility in more concentrated electrolytes. Hence, the $C(K^+)$ dependence of $j$(CO) is not monotonic and depends simultaneously on numerous competing factors that are challenging to isolate experimentally. In future work, rotating disk electrode experiments could help disentangle their individual contributions.

Table S3. Post-electrolysis ICP-OES analysis. Concentrations of trace metal impurities measured in electrolyte samples collected after the 3 h potentiostatic experiments corresponding to Figure 1.

| | Measured metal content [µg/L] in unpurified electrolytes of various *C*($KHCO_3$) | | | | |
|---|---|---|---|---|---|
| **Metal** | **0.1 M** | **0.3 M** | **0.5 M** | **0.7 M** | **1 M** |
| **Cu** | 2.99 | 2.66 | 4.18 | 1.46 | 13.10 |
| **Ni** | 0.43 | 0.29 | 0.38 | 2.95 | -0.07 |
| **Fe** | 7.75 | 7.40 | 6.87 | 7.83 | 10.38 |
| **Ag** | 1.29 | -0.12 | 2.26 | 1.90 | 2.13 |

See Figure S20 for indications of measurement standard deviation as a function of concentration. For Cu, this means levels at or below ~2 µg/L are subject to significant variance (standard deviation ≥50%) due to sensitivity of the method.

Table S4. ICP-OES quantification of trace Cu in as-prepared electrolytes (either Chelex-purified or unpurified), plus some purified then intentionally dosed with Cu (nominally 20 µg/L) (as described in Supplementary Note 1). Electrolytes of lower Cu content were prepared by dilution of these Cu stock solutions.

| **Sample** | **Cu concentration [µg/L]** |
|---|---|
| purified 0.1 M $KHCO_3$ | n.a. |
| purified 0.5 M $KHCO_3$ | 0.38 |
| purified 1 M $KHCO_3$ | 0.89 |
| unpurified 2.23 M $KHCO_3$ | 24.85 |
| 0.1 M $KHCO_3$ (purified) + 20 µg/L Cu | 17.3 |
| 0.5 M $KHCO_3$ (purified) + 20 µg/L Cu | 20.2 |
| 1 M $KHCO_3$ (purified) + 20 µg/L Cu | 21.7 |

See Figure S20 for indications of measurement standard deviation as a function of concentration. For Cu, this means levels at or below ~2 µg/L are subject to significant variance (standard deviation ≥50%) due to sensitivity of the method.

**Table S5.** Surface strain, surface and sub-surface *d*-band centers and formation energies on considered models. Supercell extensions: (111) p(3×3).

| System | Strain (%) | $\varepsilon_d - E_{Fermi}$ (eV) | | $\Delta E$ (eV) | | | | | |
|---|---|---|---|---|---|---|---|---|---|
| | | Surface | Sub-surface | CO | CHO | COCOH | COCO | H | CHO-CO |
| Ag | - | –3.89 | –4.07 | +0.43 | +0.75 | +1.65 | +0.89 | +0.58 | +0.32 |
| $Cu_{ML}Ni$ | –2.49 | –2.17 | –1.51 | –0.14 | +0.39 | +0.79 | +1.35 | +0.28 | +0.52 |
| Cu | +0.00 | –2.29 | –2.56 | –0.12 | +0.42 | +0.78 | +1.36 | +0.31 | +0.54 |
| $Cu_{ML}Pd$ | +7.76 | –1.64 | –1.80 | –0.35 | +0.28 | +0.50 | +1.01 | +0.35 | +0.62 |
| $Cu_{ML}Pt$ | +8.59 | –1.75 | –2.46 | –0.53 | +0.10 | +0.15 | +0.76 | +0.14 | +0.63 |
| $Cu_{ML}Au$ | +13.02 | –1.85 | –3.53 | –0.56 | +0.11 | +0.10 | +0.47 | +0.15 | +0.67 |
| $Cu_{2/3ML}Ag$ | +13.30 | –1.93 | –4.10 | –0.35 | +0.14 | +0.58 | +0.87 | +0.31 | +0.49 |
| $Cu_{ML}Ag$ | +13.30 | –4.10 | –0.33 | –0.33 | +0.26 | +0.15 | +0.73 | +0.27 | +0.59 |

**Table S6.** Fit parameters of linear correlation of CO formation energy ($\Delta E_{*CO}$) vs d-band center and strain (Equation 1).

| $\Delta E^{0}_{*CO}$ (eV) | $b_1$ (–) | $b_2$ (eV / %) | $R^2$ | $\chi^2$ |
|---|---|---|---|---|
| –0.91 ± 0.18 | +0.35 ± 0.07 | +0.014 ± 0.008 | 0.94 | 1.1E–02 |

**Table S7.** Fit parameters of Linear Scaling Relationships reported in Figure S12.

| | a (eV) | b (–) | $R^2$ | $\chi^2$ |
|---|---|---|---|---|
| $\Delta E_{*CHO}$ (eV) | 0.4774 ± 0.0094 | 0.66 ± 0.02 | 0.99 | 2.0E–03 |
| $\Delta E_{*COCOH}$ (eV) | 0.95 ± 0.06 | 1.59 ± 0.16 | 0.95 | 9.2E–02 |
| $\Delta E_{*H}$ (eV) | 0.39 ± 0.03 | 0.41 ± 0.07 | 0.88 | 1.5E–02 |

**Table S8.** Formation energy of Cu adatom on Cu(111) and Ag(111) substrates for 1 ML and 2/3 ML.

| System | $\Delta E_{form}$ / $N_{Cu}$ (eV) |
|---|---|
| Cu(111) | –3.8 |
| $Cu_{ML}Ag(111)$ | +0.6 |
| $Cu_{2/3ML}Ag(111)$ | +1.1 |

**Table S9:** Surface strain, surface and sub-surface d-band centers and *CO formation energies on different Ag, Cu, $Cu_{ML}Ag$ facets.

| System | Strain(%) | $\varepsilon_d - E_{Fermi}$ surf (eV) | $\varepsilon_d - E_{Fermi}$ sub-surf (eV) | $\Delta E_{*CO}$ (eV) |
|---|---|---|---|---|
| Ag(111) | - | –3.89 | –4.07 | +0.43 |
| Ag(100) | - | –3.80 | –4.03 | +0.41 |
| Ag(110) | - | –3.86 | –4.08 | +0.32 |
| Ag(211) | - | –3.89 | –4.08 | +0.45 |
| Cu(111) | +0.00 | –2.29 | –2.56 | –0.12 |
| Cu(100) | +0.00 | –2.17 | –2.57 | –0.21 |
| Cu(110) | +0.00 | –2.24 | –2.58 | –0.26 |
| Cu(211) | +0.00 | –2.27 | –2.54 | –0.10 |
| $Cu_{ML}Ag$(111) | +6.42 | –1.93 | –4.10 | –0.32 |
| $Cu_{ML}Ag$(100) | +13.28 | –1.83 | –4.14 | –0.33 |
| $Cu_{ML}Ag$(110) | +13.28 | –1.91 | –4.07 | –0.24 |
| $Cu_{ML}Ag$(211) | –2.66 | –2.00 | –4.07 | –0.14 |

**Table S10.** Summary of published studies on Ag-based $CO_2R$, demonstrating the corresponding electrode preparation methods, reaction conditions, and the reported Faradaic efficiencies for $CH_4$ production.

| Material | Pre-treatment | Cell type | Electrolyte | Potential / current | $CH_4$ quant. |
|---|---|---|---|---|---|
| Ag metal electrode[6] | Electropolish | H-Cell with CEM | 0.1 M $KHCO_3$ | -1.37 V vs NHE | FE=0 |
| Ag oxide[7] | Rolling Ag foil (>99.99 wt%), then oxidize in 0.2 M NaOH | Two compartment cell with CEM | 0.1 M $KHCO_3$ | -0.8 V vs. NHE | n.a. |
| Ag coated PVDF-based GDE[8] | n.a. | Flow cell with CEM | 1 M $KHCO_3$ | 100 mA/cm$^2$ | FE≈10% |
| Ag film on GDE[9] | n.a. | PTFE flow cell | KOH (0.1 M to 11 M) | 300 mA/cm$^2$ | n.a. |
| Polycrystalline Ag electrode/ Ag nanoparticle electrode on GDE[10, 11] | Mechanically polished, etched in $H_2SO_4$/ no treatment on GDE | Two compartment cell with AEM | 0.5 M $KHCO_3$ | -0.4 V to -0.6 V vs. RHE | n.a. |
| Ag plate[12] | n.a. | Undivided cell with 30 bar pressure | 0.2 M $K_2SO_4$ | -12 mA/cm$^2$ | FE=4% |
| Ag nanoporous electrode[13] | CV pre-treatment between +0.5 and -0.4 V vs. RHE with 0.1 V/s for 20 times in Ar purged $H_2SO_4$ | Two compartment cell with nylon membrane filter | 0.1 M $NaHCO_3$ | From ≈-0.3 V to ≈-1 V | n.a. |
| Ag foil (99.998%)[14] | Mechanically polished, rinsed with water | Custom two compartment cell with AEM | 0.1 M $KHCO_3$ | From -0.6 V to -1.4 V vs. RHE | FE≈0.1% at -1.4 V vs. RHE |
| Ag foil / Ag foam[15] | Boiling in $H_2O$ / Electrodeposition on Ag foil. | Teflon cell with CEM | 0.5 M $KHCO_3$ | -0.3 V to -1.6 V vs. RHE | @-1.5 V FE≈0% / FE≈50% |

**References**


(1) Zheng, W. iR Compensation for Electrocatalysis Studies: Considerations and Recommendations. *ACS Energy Letters* **2023**, *8* (4), 1952-1958. DOI: https://doi.org/10.1021/acsenergylett.3c00366.

(2) Son, Y. J.; Marquez, R. A.; Kawashima, K.; Smith, L. A.; Chukwuneke, C. E.; Babauta, J.; Mullins, C. B. Navigating iR Compensation: Practical Considerations for Accurate Study of Oxygen Evolution Catalytic Electrodes. *ACS Energy Letters* **2023**, *8* (10), 4323-4329. DOI: https://doi.org/10.1021/acsenergylett.3c01658.

(3) Heenan, A. R.; Hamonnet, J.; Marshall, A. T. Why Careful iR Compensation and Reporting of Electrode Potentials Are Critical for the CO2 Reduction Reaction. *ACS Energy Letters* **2022**, *7* (7), 2357-2361. DOI: https://doi.org/10.1021/acsenergylett.2c00800.

(4) Zheng, Z.; Yao, Y.; Yan, W.; Bu, H.; Huang, J.; Ma, M. Mechanistic Insights into the Abrupt Change of Electrolyte in $CO_2$ Electroreduction. *ACS Catalysis* **2024**, *14* (8), 6328-6338. DOI: https://doi.org/10.1021/acscatal.4c00869.

(5) Lorenzutti, F.; Seemakurthi, R. R.; Johnson, E. F.; Morandi, S.; Nikačević, P.; López, N.; Haussener, S. Microenvironment effects in electrochemical $CO_2$ reduction from first-principles multiscale modelling. *Nature Catalysis* **2025**, *8* (9), 905-918. DOI: https://doi.org/10.1038/s41929-025-01399-2.

(6) Yoshio Hori, H. W., Toshio Tsukamoto and Osamu Koga. Electrotatalytic Process of CO selectivity in Electrochemical Reduction of $CO_2$ at Metal Electrodes in Aqueous Media. *Electrochimica Acta* **1993**, *39*, 1833-1839. DOI: https://doi.org/10.1016/0013-4686(94)85172-7.

(7) Yang, M.; Wu, J.; Li, Y.; Pan, H.; Cui, H.; Lu, X.; Tang, X. Structural Evolution of Oxide-Derived Nanostructured Silver Electrocatalysts during $CO_2$ Electroreduction. *ACS Catalysis* **2024**, *14* (8), 6169-6178. DOI: https://doi.org/10.1021/acscatal.4c00217.

(8) Senocrate, A.; Bernasconi, F.; Rentsch, D.; Kraft, K.; Trottmann, M.; Wichser, A.; Bleiner, D.; Battaglia, C. Importance of Substrate Pore Size and Wetting Behavior in Gas Diffusion Electrodes for $CO_2$ Reduction. *ACS Applied Energy Materials* **2022**, *5* (11), 14504-14512. DOI: https://doi.org/10.1021/acsaem.2c03054.

(9) Seifitokaldani, A.; Gabardo, M. C.; Burdyny, T.; Dinh, C.-T.; Edwards, P. J.; Kibria, G. M.; Bushuyev, S. O.; Kelley, O. S.; Sinton, D.; Sargent, H. E. Hydronium-Induced Switching between $CO_2$ Electroreduction Pathways. *Journal of the American Chemical Society* **2018**, *140* (11), 3833-3837. DOI: https://doi.org/10.1021/jacs.7b13542.

(10) Lu, Q.; Rosen, J.; Zhou, Y.; Hutchings, G. S.; Kimmel, Y. C.; Chen, J. G.; Jiao, F. A selective and efficient electrocatalyst for carbon dioxide reduction. *Nat Commun* **2014**, *5*, 3242. DOI: https://doi.org/10.1038/ncomms4242 From NLM PubMed-not-MEDLINE.

(11) Rosen, J.; Hutchings, G. S.; Lu, Q.; Rivera, S.; Zhou, Y.; Vlachos, D. G.; Jiao, F. Mechanistic Insights into the Electrochemical Reduction of $CO_2$ to CO on Nanostructured Ag Surfaces. *ACS Catalysis* **2015**, *5* (7), 4293-4299. DOI: https://doi.org/10.1021/acscatal.5b00840.

(12) Proietto, F.; Berche, F.; Galia, A.; Scialdone, O. Electrochemical conversion of pressurized CO2 at simple silver-based cathodes in undivided cells: study of the effect of

pressure and other operative parameters. *Journal of Applied Electrochemistry* **2020**, *51* (2), 267-282. DOI: https://doi.org/10.1007/s10800-020-01505-1.

(13) Huang, J.-F.; Wu, Y.-C. Tunable Ag Micromorphologies Show High Activities for Electrochemical H2 Evolution and $CO_2$ Electrochemical Reduction. *ACS Sustainable Chemistry & Engineering* **2019**, *7* (6), 6352-6359. DOI: https://doi.org/10.1021/acssuschemeng.9b00116.

(14) Hatsukade, T.; Kuhl, K. P.; Cave, E. R.; Abram, D. N.; Jaramillo, T. F. Insights into the electrocatalytic reduction of $CO_2$ on metallic silver surfaces. *Phys Chem Chem Phys* **2014**, *16* (27), 13814-13819. DOI: https://www.ncbi.nlm.nih.gov/pubmed/24915537 From NLM PubMed-not-MEDLINE.

(15) Dutta, A.; Morstein, C. E.; Rahaman, M.; Cedeño López, A.; Broekmann, P. Beyond Copper in $CO_2$ Electrolysis: Effective Hydrocarbon Production on Silver-Nanofoam Catalysts. *ACS Catalysis* **2018**, *8* (9), 8357-8368. DOI: https://dx.doi.org/10.1021/acscatal.8b01738.